Direct Electrodeposition of Electrically Conducting Ni 3 (HITP) 2 MOF Nanostructures for Micro-Supercapacitor Integration

Sepideh Behboudikhiavi, Géraldine Chanteux, Binson Babu, Sébastien Faniel, Florent Marlec, Kevin Robert, Delphine Magnin, Fabio Lucaccioni, Joel Ojonugwa Omale, Petru Apostol, et al.

Direct Electrodeposition of Electrically Conducting $Ni_3(HITP)_2$ MOF Nanostructures for Micro-Supercapacitor Integration

*Sepideh Behboudikhiavi[a]‡, Géraldine Chanteux[a]‡, Binson Babu[a], Sébastien Faniel[b], Florent Marlec[c,d], Kevin Robert[c,d], Delphine Magnin[a], Fabio Lucaccioni[a], Joel Ojonugwa Omale[a], Petru Apostol[a], Luc Piraux[a], Christophe Lethien[c,d,e], and Alexandru Vlad[a]**

A. Dr. S. Behboudikhiavi, G. Chanteux, Dr. B. Babu, Dr. D. Magnin, F. Lucaccioni, J. O. Omale, Dr. P. Apostol, Prof. L. Piraux, Prof. A. Vlad

Institute of Condensed Matter and Nanosciences, Université Catholique de Louvain

1348, Louvain-la-Neuve, Belgium

E-mail: alexandru.vlad@uclouvain.be

B. Dr. S. Faniel

Institute for Information and Communication Technologies, Electronics and Applied Mathematics, Université catholique de Louvain

1348, Louvain-la-Neuve, Belgium

C. F. Marlec, K. Robert, Prof. C. Lethien

Institut d'Electronique, de Microélectronique et de Nanotechnologies, Université de Lille, CNRS, Université Polytechnique Hauts-de-France, UMR 8520 – IEMN

59000, Lille, France

D. F. Marlec, K. Robert, Prof. C. Lethien

Réseau sur le Stockage Electrochimique de l'Energie (RS2E), CNRS FR 3459

33 rue Saint Leu

80039, Amiens Cedex, France

E. Prof. C. Lethien

Institut Universitaire de France (IUF),

Saint-Michel 103

75005, Paris, France

‡ Equal contribution

Keywords: non-sacrificial; anodic electrodeposition; micro-supercapacitor; MOFs nanostructure

Abstract: Micro-supercapacitors emerge as an important electrical energy storage technology expected to play a critical role in the large-scale deployment of autonomous microdevices for health, sensing, monitoring, and other IoT applications. Electrochemical double-layer capacitive storage requires a combination of high surface area and high electronic conductivity, with these being attained only in porous or nanostructured carbons, and recently found also in conducting metal-organic frameworks. However, techniques for conformal deposition at micro- and nanoscale of these materials are complex, costly, and hard to upscale. Herein, we report direct, one step non-sacrificial anodic electrochemical deposition of Ni_3(2,3,6,7,10,11-hexaiminotriphenylene)$_2$ - $Ni_3(HITP)_2$, a porous and electrically conducting metal-organic framework. Employing this strategy enables the growth of $Ni_3(HITP)_2$ films on a variety of 2D substrates as well as on 3D nanostructured substrates to form $Ni_3(HITP)_2$ nanotubes and Pt@ $Ni_3(HITP)_2$ core-shell nanowires. Based on the optimal electrodeposition protocols, $Ni_3(HITP)_2$ films interdigitated micro-supercapacitors are fabricated and tested as a proof of concept.

Introduction

Electrically conducting metal-organic frameworks (MOFs) are a class of materials of particular interest for energy storage applications requiring fast charging (*i.e.* electrochemical capacitor) due to their potential to attain high surface area exceeding 1.000 $m^2.g^{-1}$ and electrical conductivity up to 10^3 $S.cm^{-1}$.[1–5] Considering the increasing demand for wearable devices, microelectronics, and IoT applications, miniaturization of energy storage devices is essential, and micro-supercapacitors appear to be excellent candidates due to their high power density and long cycle lifetime.[6–9] However, the energy density remains low due to the limited double-layer capacitive storage mechanism as well as reduced size and low active material mass loading.[10–13] To improve the energy density, one of the strategies is to utilize pseudocapacitive materials such as conducting polymers[14,15], metal oxides[16–19], metal nitride[20–22], however at the expense of power density or cycling stability. Owing to the high conductivity, higher surface, and controllable porosity, conductive MOFs have emerged over the past years as excellent candidates for fabricating high-energy supercapacitors without compromising on power density

and cycling stability.[4,23] Hence, growing thin films of electrically conducting MOFs is considered as one key solution to tackle this challenge.[24–26]

However, conductive MOFs are typically synthesized in the form of polycrystalline or single-crystal bulk powder form, by means of various techniques such as diffusion (including mild and solvothermal conditions), microwave assisted, mechanochemical, and electrochemical methods.[27] Given the bulk nature of nucleation and growth process, these conventional methods are difficult to adapt for the preparation of controlled nanostructures, or conformal and selected area thin film coating. A significant effort has thus been devoted to elaborating on various techniques for film growth or integration of conducting (as well as non-conducting) MOFs on solid substrates. These include exfoliation and reassembly[28], liquid phase epitaxy[29], gas-liquid phase interfacial[3,30], Langmuir-Blodgett layer-by-layer deposition[31], chemical vapor deposition[32,33], electrochemical synthesis[34], and electrodeposition [24–26]. However, except for electrodeposition, these techniques are time and resource consuming deriving from the lack of precise controllability of growth kinetics and low reproducibility. Additionally, some methods cannot be applied to certain classes of MOF, given the requirements of the deposition methods (*e.g.* volatile precursors, thermal or chemical stability).

Electrochemical deposition is a well-established thin film growth method, that has been extensively researched over the past century and is now firmly consolidated in industrial processes such as refining, electro-winning, and electroplating. A variety of materials can be synthesized by electrodeposition, for instance, metals, alloys, polymers, oxides; with also various morphologies, like thin film, nanoparticles, nanorods and nanowires, *etc*.[35] Electrochemical deposition critically enables well-tuned and large-area conformal thin films coatings of various insulating or conducting films on versatile conducting substrates with complex geometries.[18,19,24,36] The method can be conducted in mild conditions thus allowing the deposition of conformal and uniform films with various morphologies through adjustment of the parameters of electrodeposition.[27,37–39]

The MOF electrodeposition techniques can be divided into cathodic or anodic processes. The former[40] has been dominantly employed to produce thin films of non-conductive MOFs, for instance, $Zn_4O(BDC)_3$[41,42] and Cu-BTC[43]. The underlying mechanism relies on the electrochemical reduction of sacrificial chemical species (pro bases) such as NO_3^- and H_2O_2, generating OH^- to deprotonate the linker, resulting in MOF chemical deposition on the cathode surface. The cathodic deposition has been largely applied for the synthesis of non-conductive MOFs, and only few reports describing the cathodic deposition of Cu catecholate conducting MOFs can be found.[44] In comparison, the anodic deposition proved to be more versatile and

has been applied for the synthesis of both, insulating and conducting MOF films.[45–50] However, both methods as specifically applied to MOF growth have a series of technical and practical intrinsic limitations. For instance, metallic impurities may be incorporated into the MOF by either electrochemical reduction of metal ions (in the cathodic process) or from remaining domains of the sacrificed metallic anode (in the anodic process).[42] Controlled deposition of MOF nanostructures (nanowires, nanotubes inside a template for example), or functionalization of nanostructured metal films (*e.g.* core-shell nanowires or simply growth on patterned metallic micro- or nano-electrodes) remains scarcely feasible given the particular conditions used in the developed approaches. Therefore, the challenge is to elaborate a non-sacrificial method to obtain highly pure conductive MOF films on 2D and 3D substrates.

Worth being mentioned also the mechanism particularities of these methods. The conventional anodic deposition of MOF is based on first step anodic generation of metal cations (by corrosion from the working substrate electrode) in an electrolytic bath containing the ligand and specific additives (Scheme 1A). Metal cations then diffuse and react with linker to yield the MOF. This process however decouples the intrinsic electron conducting property of a conducting MOF from the electrodeposition charge transfer step and interface. In fact, these will take place at the metal electrode – electrolyte interface (Scheme 1B),[51] with the MOF growth however proceeding at the MOF-electrolyte interface, by the metal cation diffusion. This is partially counterintuitive, as one would expect that charge transfer and material growth to take place at the same interface, as it is the case for all previously deposited conducting materials (*e.g.* metals, semiconductors, conducting polymers). Surprising as it may sound, direct and non-sacrificial electrochemical deposition of conducting MOFs thus far has little benefited from this intrinsic property.

Here, we report a one-step, non-sacrificial anodic electrochemical deposition of Ni_3(2,3,6,7,10,11-hexaiminotriphenylene)$_2$ electronically conducting MOF (Scheme 1A). The spontaneous oxidation of the ligand step, attributed to the molecular oxygen from air is replaced by a controlled electrochemical oxidation (under Argon atmosphere) of the ligand. A precise control over electrochemical parameters was required to ensure the growth of $Ni_3(HITP)_2$ films with targeted thickness. The electrochemical behaviour of all chemical species present in the air-free electrolytic bath were first analysed separately and then combined all together to understand the redox activities. Based on the analysis of the electrolytic bath components, the non-sacrificial anodic deposition of $Ni_3(HITP)_2$ was then optimized in an air-free electrolytic bath in both aqueous-based (H_2O-DMF-DMA) and organic (MeOH-DMSO) electrolytic solutions. The thickness, morphology, and phase purity of the films are tuneable by the

deposition parameters such as pulsed, continuous potentiostatic, or potentiodynamic (CV) conditions, the maximal amount of applied charge, the chemical composition of the electrolytic bath, and the deposition time. The optimization of different parameters enabled the deposition of $Ni_3(HITP)_2$ thin films on various conductive substrates (metals, carbon semiconductors) of different geometries leading to different morphologies of the $Ni_3(HITP)_2$ films (planar surfaces, nanowire, nanotube and porous networks, core-shell architectures and interdigitated structures). Finally, the deposition method was integrated as a facile pragmatic technique to fabricate micro-supercapacitors based on $Ni_3(HITP)_2$ functionalized interdigitated electrodes with high areal capacitance and long-term cycling stability. To be mentioned, in the final stage of preparation of this work, a complementary development was reported by Lu *et al*[52], wherein anodic electrochemical-chemical deposition of catecholate-based MOF in aqueous electrolytic bath was realized on various substrates and of nanostructures. Our work extends the applicability to amine-based MOF in both aqueous-based and organic electrolytic bath, with micro-supercapacitor device integration, with both developments thus validating and consolidating the universality of non-sacrificial anodic electrodeposition of electrically conducting MOFs.

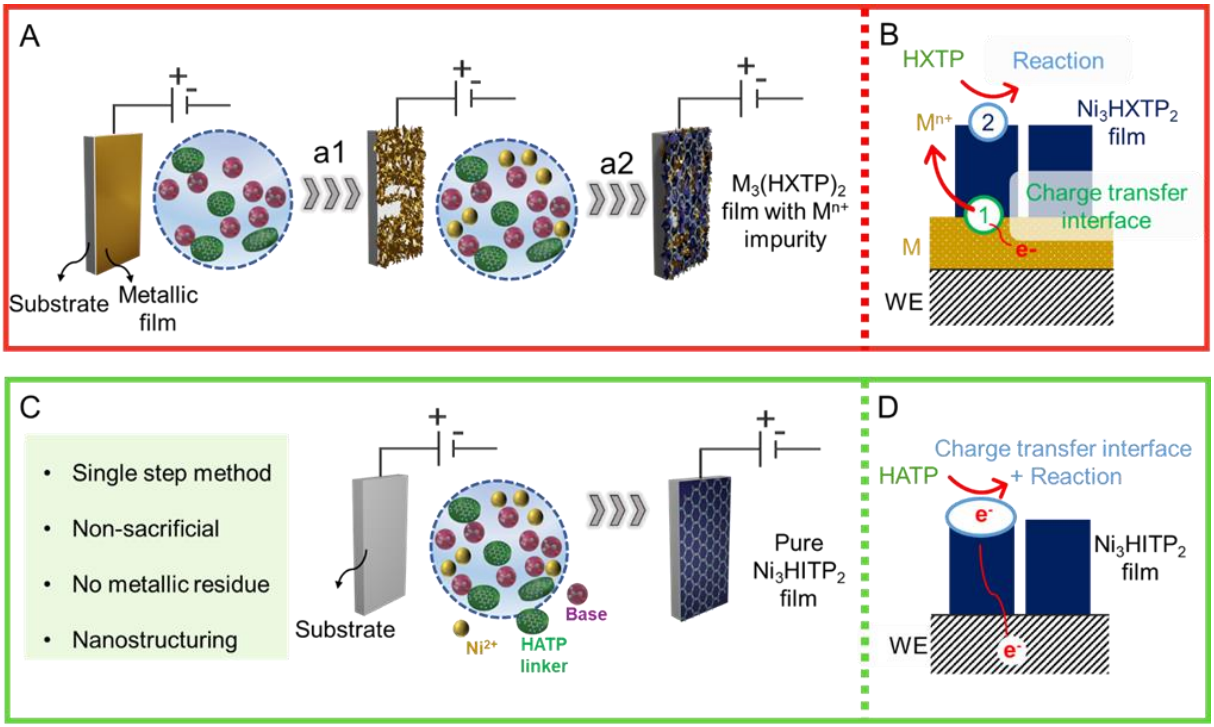

Scheme 1. Schematics of (A) the anodic sacrificial electrodeposition with (B) the corresponding growth mechanism with decoupled charge transfer and reaction interfaces, as compared to (C) direct non-sacrificial electrochemical deposition method for $Ni_3(HITP)_2$ applied in this work and the corresponding (D) growth mechanism at the interface.

Results and discussion

The anodic electrodeposition procedure for $Ni_3(HITP)_2$ is schematized in Scheme 1C. The electrodeposition of $Ni_3(HITP)_2$ from an electrolytic bath including all precursors (*i.e.* HATP ligand, base, and Ni^{2+} ions) can mitigate all the challenges related to the sacrificial anodic dissolution of metallic Ni film as the source of metallic cations. The growth and charge transfer thus simultaneously take place at the MOF electrode - electrolyte interface (Scheme 1D). Accordingly, this method is expected to entail the local generation of electrochemically oxidized HATP ligand through charge transfer interface, followed by the formation of $Ni_3(HITP)_2$ film at the exact same interface, as it is the case for conventional electrodeposition of conducting materials (*e.g.* metals, semiconductors, conducting polymers).

The challenging feature in the electrodeposition of $Ni_3(HITP)_2$ is that the reactant mixture, or the electrolytic bath, is not stable under ambient air conditions. In fact, the molecular oxygen (O_2) is a co-reactant in the $Ni_3(HITP)_2$ formation reaction, by oxidizing the deprotonated HATP ligand. Subsequently, the oxidized ligand undergoes a series of reactions implying Ni^{2+} coordination and acid-base reactions, to form the $Ni_3(HITP)_2$ MOF with diiminobenzosemiquinoate submoieties, following one of the three reaction pathways displayed in Figure 1A (essentially depending on the composition of the electrolytic bath - amount of Ni^{2+}, HATP and basic species).[53–56] Thus, our rationale was to eliminate the molecular oxygen from the electrolytic bath, and activate this initial anodic step electrochemically (Figure 1A). To attest this, the lower coordination ability of the $(diamino)_2$-Ni, relative to the $(diimino)_2$-Ni moieties, was first elucidated. For instance, all constituents including HATP.6HCl, Ni^{2+} and a large excess of NaOAc were added to a deaerated H_2O-DMF-DMA mixed solvent.[57] Upon heating at 80 °C and keeping the reaction mixture under inert atmosphere, no reaction took place and the electrolytic bath remained unchanged for more than 2 hours (Figure S1-A). On the contrary, the formation of $Ni_3(HITP)_2$ was promptly discerned upon exposing the mixture to ambient air conditions (*i.e.* O_2 diffusion and reaction, Figure S1-B).

Next, a series of control experiments were performed to elucidate the role of individual electrolytic bath constituents (Figure 1B). In an electrolyte comprising only Ni^{2+} salt, no redox process was observed within the studied potential window from -0.5 up to 1.0 V (*vs.* Ag pseudo-reference), consistent with the anodic stability of Ni^{2+}. Instead, HATP manifested a sharp anodic process at ~ 0.3V *vs.* Ag, representative of the redox of similar *o*-benzenediamine species,[58,59] and consistent with the theoretical potential of ~0.30V. The low anodic stability of deprotonated HATP in solution is also in agreement with its reactivity towards molecular O_2. The tail on the anodic wave can be explained by the subsequent formation of complex species, potentially arising from the supramolecular packing of the oxidized deprotonated ligand

(through π-π stacking, that could supposedly form rigid molecular columns)[60] and more likely *via* aromatization and polymerization chain reactions (resulting in phenazine or 1,4-benzoquinone-diimine - type polymers). The process is irreversible as no associated cathodic process could be observed. This is explained by the basic conditions (pH ~9) of the electrolytic bath, wherein the oxidized HATP and HATP participate in chemical reactions (dimerization and polymerization).[58]

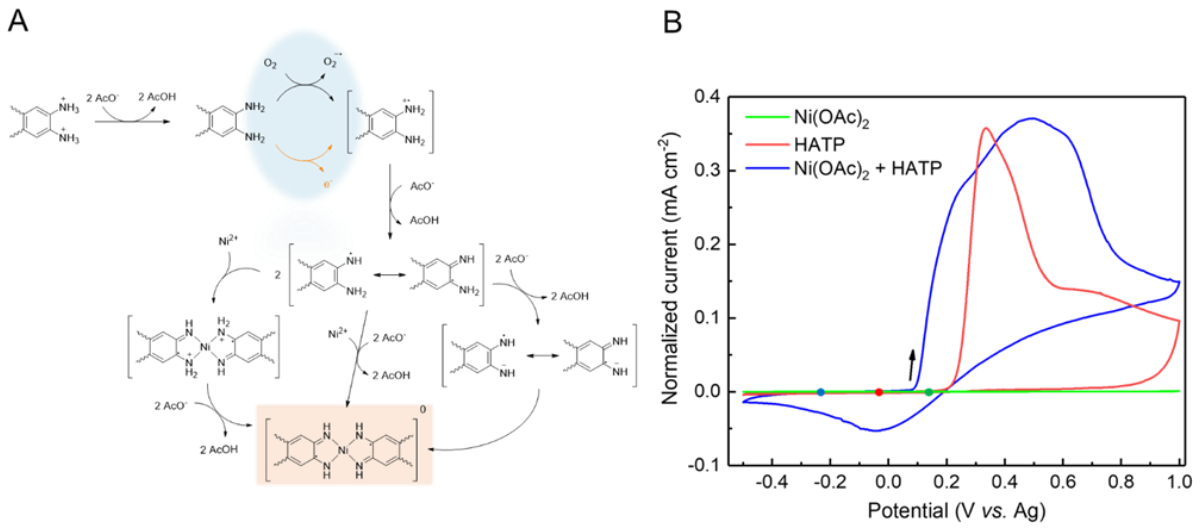

Figure 1. (A) The mechanism of $Ni_3(HITP)_2$ synthesis implying initial HATP ligand chemical or electrochemical oxidation, followed by a series of acid-base and coordination reactions. (B) Cyclic voltammograms of individually containing $Ni(OAc)_2$ and HATP solutions, as compared to the $Ni_3(HITP)_2$ precursors electrolytic bath, all acquired at a scan rate of 10 $mV.s^{-1}$ on ITO working electrode.

In presence of both components, HATP and $Ni(OAc)_2$, the anodic peak is broadening, concomitant with an earlier onset of oxidation and an associated reduction peak at ~ -0.05V vs Ag in the reverse scan (Figure 1B). The oxidation onset at 0.05V is interpreted as the oxidation of HATP, facilitated (i.e. stabilized) by the subsequent coordination reaction with Ni^{2+}. The anodic peak broadening is attributed to the emergence and deposition of more intricate entities, such as coordinated Ni^{2+} ions with the oxidized hexaiminotriphenylene (small and long chain $Ni_3(HITP)_2$ species) or ligand-based polymers, processes dependent on HATP oxidation conditions and Ni^{2+} coordination kinetics.[58] The reduction peak in the reverse scan is associated to the reduction of the formed and oxidized species, including redox of $Ni_3(HITP)_2$ (as afterwards exploited for pseudocapacitive storage, see discussion and results in next sections). A comparable electrochemical behaviour was previously observed by Pelmus *et al.* for the 1,4-diaminobenzene organic compound.[59] To be noted that already after the first cyclic

voltammetry (CV) scan, a thin film of dark blue translucent reflection covered the working electrode surface, corresponding to the $Ni_3(HITP)_2$ deposits confirming the charge passed during the electrodeposition process (Figure S2-A).

Methods and conditions were next optimized to establish the optimal deposition parameters. Both cyclic voltammetry and potentiostatic (continuous or pulsed potential) electrodeposition techniques were selected and tested. In the cyclic voltammograms using the MeOH-DMSO electrolytic bath (Figure 2A), a gradual reduction of the anodic current was accompanied by a peak shifting towards higher potentials. This is explained by the progressive nucleation and growth of the less conductive $Ni_3(HITP)_2$ on the surface of ITO,[61] resulting in partial surface passivation, decreased current density and increased polarization, as also confirmed by SEM analysis of the ITO surface after individual CV scans (Figure 2B). Regarding the top surface SEM imaging, a Volmer Veber island growth mode seems to be involved in the electrodeposition process of MOF.[62] After several CV cycles (typically more than 10), the anodic electrodeposition current became low indicating a self-limiting growth, consistent with the observations on benzene-1,4-diamine electrochemical studies by Pelmus *et al.*[59] Constant potential anodic electrodeposition was also studied. Both, aqueous based (H_2O-DMA-DMF) and organic (MeOH-DMSO) electrolytic baths were tested. First, a wide potential window was applied, in accordance with cyclic voltammograms for each specific condition (Figure S3). The potentiostatic deposition (in H_2O-DMA-DMF) at 0.5 V provided the most crystalline and uniform film as corroborated by XRD analysis (Figures 3 and S4-A). Chronoamperograms for continuous and pulsed potentiostatic depositions are shown in Figure 2C. For the continuous deposition method, a rapid drop of the current density was noted, corroborating the CV analysis (Figure 1B) of gradual passivation of the surface, but also possibly originating from reactants diffusion limited process. The pulsed method manifested in turn a lower current density drop and a higher charge density on average, by allowing diffusion and replenishment of the electroactive species in the diffusion layer.

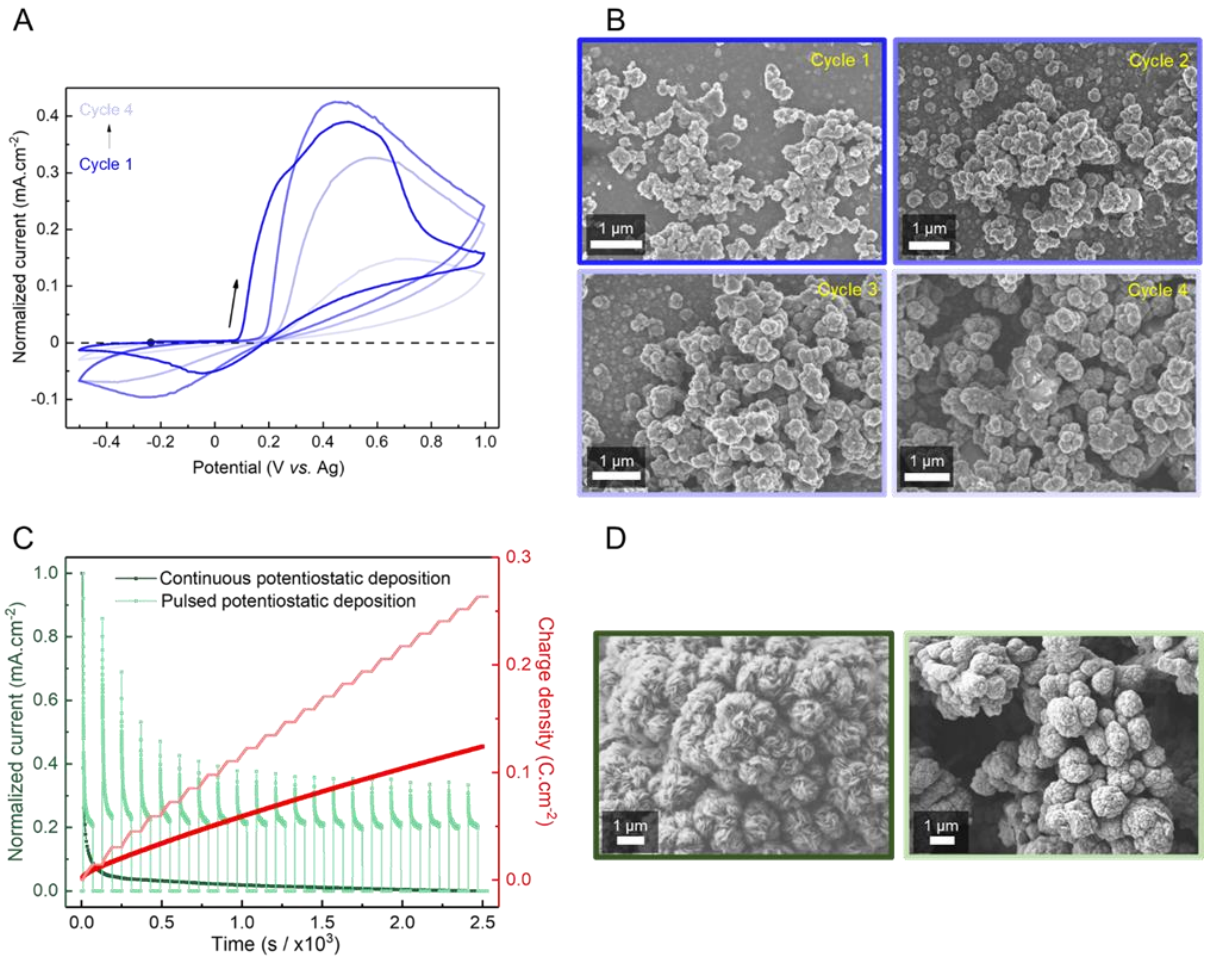

Figure 2. (A) Cyclic voltammograms using the organic-based (MeOH-DMSO) electrolytic bath recorded at a scan rate of 10 mV.s-1 on ITO substrate. (B) The SEM images of $Ni_3(HITP)_2$ deposits on ITO surface after selected cyclic voltammetry scans. (C) The chronoamperograms (normalized current density) and the corresponding cumulative deposition charge density for potentiostatic anodic deposition methods by using the continuous (dark colored line) and square pulsed (light colored line) methods (with t_{on} = 1 min, V_{on} = 0.8 V; and t_{off} = 1 min, V_{off} = open circuit voltage). (D) The corresponding SEM images of $Ni_3(HITP)_2$ deposits obtained by potentiostatic continuous (dark colored contour) and pulsed deposition (light colored contour).

In MeOH-DMSO electrolytic bath, continuous deposition of $Ni_3(HITP)_2$ resulted in a needle-shaped spherical aggregated crystalline film morphology, whereas pulsed deposition yielded a smoother spherical-based crystalline deposit (Figure 2D). The crystallites size is notably higher under continuous deposition. The opposite situation (*i.e.* smaller size of crystallites) is observed for pulsed deposition, which can be explained by limited growth and augmented nucleation and diffusion rate due to the application of t_{off}. Indeed, pulsed deposition exhibited different morphologies resulting in a more uniform film, with finer grains when $\frac{t_{on}}{t_{on}+t_{off}}$ factor was smaller – with t_{on} from 1 min to 100 ms and t_{off} from 1 min to 10 sec, respectively (Figure S5-

C and D).[63,64] In contrast, continuous potentiostatic deposition of $Ni_3(HITP)_2$ using the H_2O-DMF-DMA electrolytic bath displayed bigger lamellar spherical aggregates, with nuclei proliferating on the surface (Figure S5-A and B).

ATR-IR spectroscopy analysis indicated that films obtained by electrochemical deposition method, in both H_2O-DMF-DMA and MeOH-DMSO electrolytic baths, possess the typical signature of $Ni_3(HITP)_2$ bands, particularly with the aromatic bands in the 1200 – 1500 cm^{-1} region (Figure S6). No signatures of unreacted ligand could be detected. The X-Ray Diffraction analysis on powder (PXRD) revealed that among all methods evaluated, the most crystallized MOF films were achieved under potentiostatic conditions using the H_2O-DMF-DMA electrolytic bath, or pulsed potentiostatic conditions using the MeOH-DMSO electrolytic bath (Figure 3). All the Bragg peaks were assigned to simulated and bulk chemically synthesized $Ni_3(HITP)_2$ phase (Figure 3A-B) are clearly defined for the films obtained *via* potentiostatic (continuous and pulsed) deposition methods (Figure 3D-F).[56] The PXRD of the material prepared by potentiodynamic method did not provide any discernible crystalline phase, whereas the crystallinity of deposits derived from potentiostatic continuous deposition could be enhanced *via* pulsed deposition (Figure 3D-F). The main reasons of such differences can be explained by the lack of oxidation control as well as charge/mass transfer kinetics of the electroactive species (leading to different oxidation levels/states) under potentiodynamic deposition and species' diffusion limitations under continuous potentiostatic deposition. Accordingly, the pulsed potentiostatic deposition in MeOH-DMSO electrolytic bath was selected as the most appropriate method for further studies and device integration. No other diffraction peaks could be as well identified in the PXRD of deposits. To further prove the composition and purity of the electrodeposited $Ni_3(HITP)_2$, XPS analysis was conducted (Figure S7). The peaks in the high resolution spectrum of Ni2p (Ni2p1/2 at 854.79 eV and Ni2p3/2 at 872.38 eV) are exclusively assigned to Ni^{2+} in pure $Ni_3(HITP)_2$ without any trace of other possible parasitic species (i.e. Ni0, $Ni(OH)_2$ or NiO).

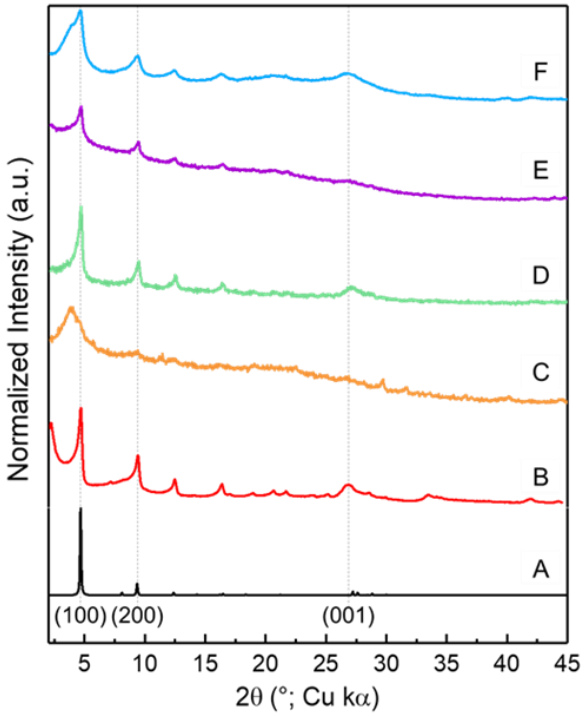

Figure 3. (A) Simulated and (B) experimental PXRD pattern of $Ni_3(HITP)_2$ made by chemical synthesis. PXRD patterns of $Ni_3(HITP)_2$ deposits obtained by (C) potentiodynamic deposition in MeOH-DMSO electrolytic bath, (D) potentiostatic deposition in H_2O-DMF-DMA electrolytic bath, (E) continuous and (F) pulsed potentiostatic deposition in MeOH-DMSO electrolytic bath.

The compatibility of the anodic deposition of MOF films on various substrates is a key aspect for advances microdevice integration. To this end, four additional conductive substrates - Pt sheet, stainless steel sheet, vanadium-nitride coated on Si/Si_3N_4 sample and carbon cloth - were tested as working current collectors for the electrodeposition of $Ni_3(HITP)_2$ films using the optimized pulsed potentiostatic method in MeOH-DMSO electrolytic bath (Figure 4). SEM analyses revealed analogous spherical aggregates morphologies on all tested substrates, echoing the resultant deposited films on ITO substrate. Specifically, the $Ni_3(HITP)_2$ deposition on vanadium-nitride current collectors appeared as a homogeneous film, punctuated by very small spherical particles smaller than 200 nm in diameter. Comparatively, the $Ni_3(HITP)_2$ deposits on other substrates are formed of bigger spherical aggregated particles, of dimensions ranging from 200 to 300 nm in diameter on carbon cloth, expanding to 1 µm diameter on stainless-steel sheet, and reaching more than 2-3 µm diameter on Pt sheet. These discrepancy in film morphology and particles diameter can be attributed to the roughness, wettability and electrocatalytic effect of each current collector, which modulate the nuclei growth and kinetics, thus dictating the texture of the $Ni_3(HITP)_2$ films.[65]

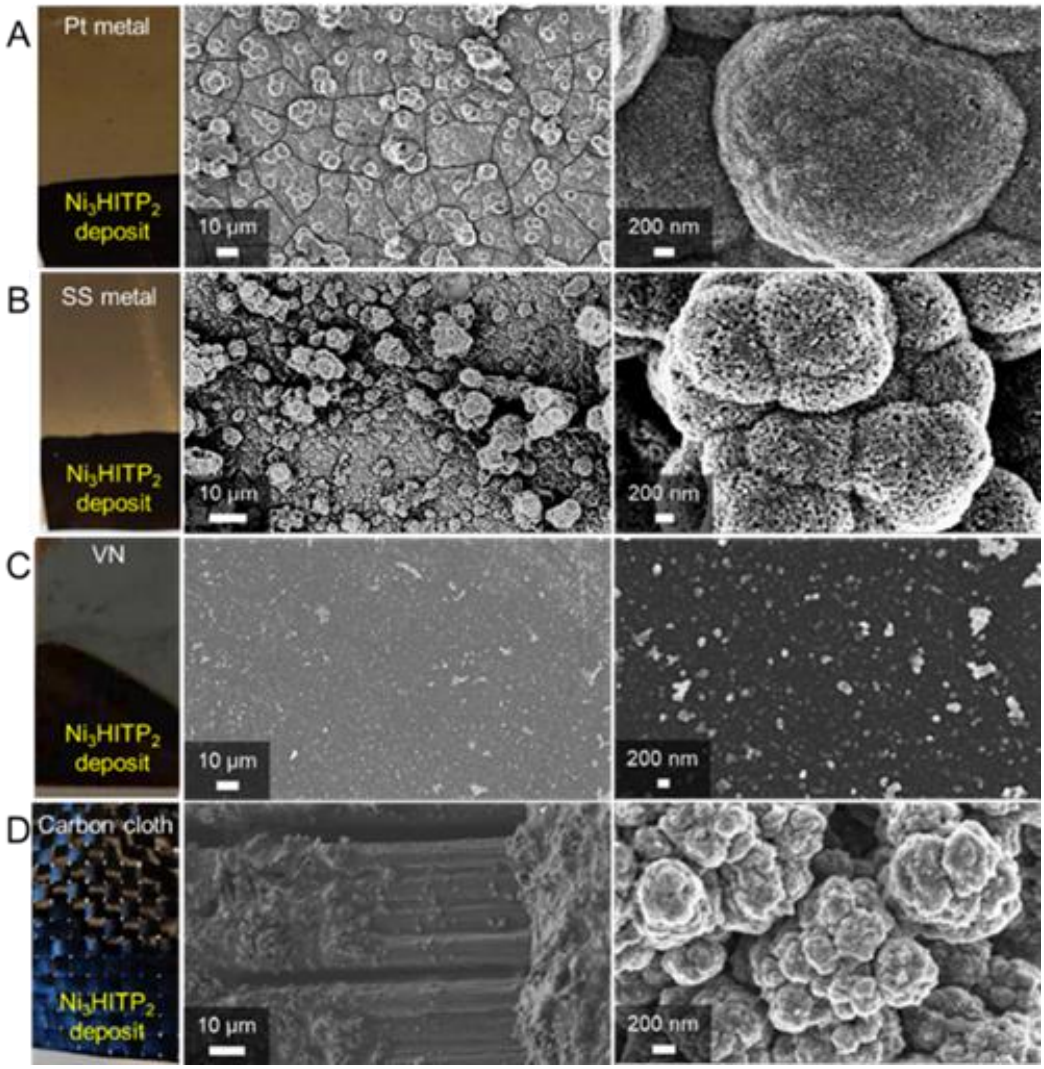

Figure 4. Optical (left) and SEM (middle and right) images of the $Ni_3(HITP)_2$ film on various substrates electrodeposited from MeOH-DMSO electrolytic bath by pulsed potentiostatic method: (A) on Pt sheet, (B) on stainless steel sheet, (C) on vanadium nitride coated on Si/Si_3N_4 substrate, and (D) on carbon cloth.

The optimized deposition method was also applied on 3D nanostructured substrates, with the aim to shape $Pt@Ni_3(HITP)_2$ core-shell nanowire (Figure 5A) and template $Ni_3(HITP)_2$ nanotube scaffolds (Figure 5B) that are expected to augment the target performances owing to the 3D nanoarchitectured scaffolds.[66–68] The potentiostatic pulsed deposition of $Ni_3(HITP)_2$ in MeOH-DMSO electrolytic bath on an interconnected Pt nanowire network substrate (Figure 5A-i.), resulted the formation of the core-shell nanostructures (Figures S8, S9). A uniform $Ni_3(HITP)_2$ shell-layer of 55 nm thickness was grown by applying a charge density of 650 $mC.cm^{-2}$. SEM unveiled the typical texture of $Ni_3(HITP)_2$ film covering the surface of each Pt nanowire (Figure 5A-ii), with the core-shell morphology confirmed by TEM (Figure 5A-iii). Similarly, the synthesis of $Ni_3(HITP)_2$ nanotubes was realized by pulsed potentiostatic

deposition using an interconnected track-etched polycarbonate template membrane (pore diameter of 230 nm). The deposition was achieved by applying the total charge of ~ 2 $C.cm^{-2}$ leading to a $Ni_3(HITP)_2$ nanotube network, as revealed after the dissolution of the template (Figure 5B). The height of scaffold network was estimated at 15 µm, displaying good mechanical robustness (Figure S10). The nanotubes have a wall thickness of 70 nm with an outer diameter of 230 nm (as replication of the template). The diffusion of reactant species within the pores acts as the rate-determining step in $Ni_3(HITP)_2$ deposition, leading to the partial filling of the pores with HATP, particularly concentrated along the peripheral walls of the pores throughout the deposition, resulting in the hollow cylindrical (nanotube) morphology.[69] Such configurations of core-shell nanowire and nanotube networks have the potential to enhance the accessibility of the $Ni_3(HITP)_2$ surface area, while shortening the diffusion path of ions as compared to the bulk film morphology. Furthermore, it can be expected that Pt@$Ni_3(HITP)_2$ nanowire network offers higher electrical conductivity and mechanical stability relative to the pure bulk $Ni_3(HITP)_2$ by the synergetic effect of combining Pt and $Ni_3(HITP)_2$ constituents in one single nanostructure.[70]

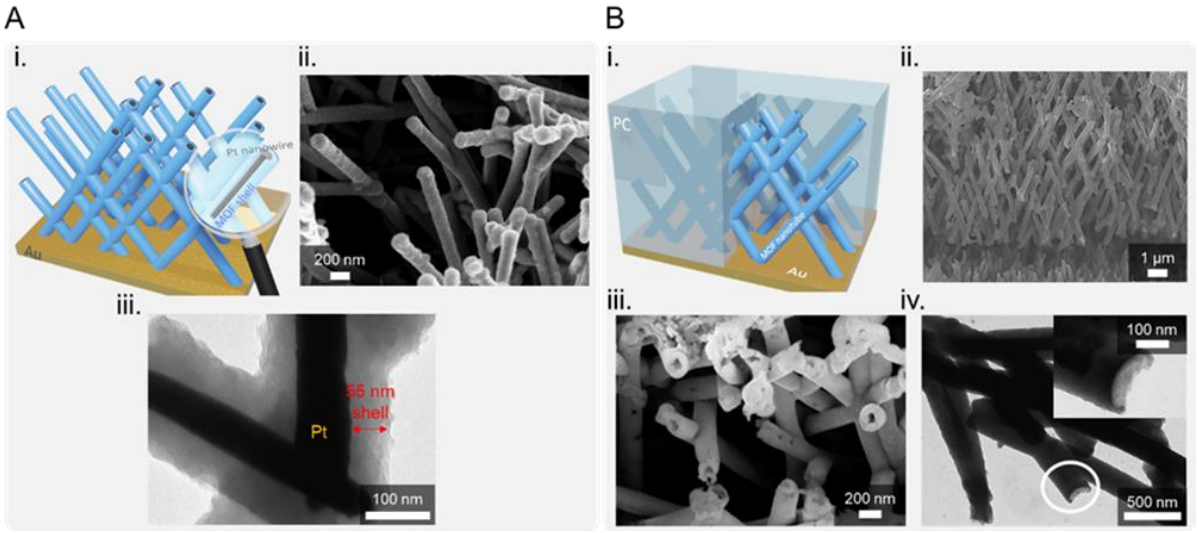

Figure 5. (A-i.) Schematic illustration of the Pt@$Ni_3(HITP)_2$ core-shell nanowire network. (A-ii) SEM image of the Pt@$Ni_3(HITP)_2$ nanowire network and (A-iii.) TEM image showing the Pt core and $Ni_3(HITP)_2$ shell composing the nanowire network. (B-i.) Schematic illustration of $Ni_3(HITP)_2$ nanotube network. (B-ii.) Wide view and (B-iii.) high resolution SEM image of the $Ni_3(HITP)_2$ nanotube network. (B-iv.) TEM image highlighting a $Ni_3(HITP)_2$ nanotube.

Pushing the concept further, $Ni_3(HITP)_2$ was deposited on Pt interdigit current collector electrodes to assemble a micro-supercapacitor (Figure 6A). The resulting microdevice made on Si wafer is composed of two Pt-$Ni_3(HITP)_2$ electrodes in an interdigit configuration. The

$Ni_3(HITP)_2$ does not display a symmetric CV profile in the working potential window. Given the capacitance attained in the forward and reverse scans of the $Ni_3(HITP)_2$ is different, charge balance between the two electrodes was attained by tuning the thickness of the MOF film. By applying different electrodeposition charge on individual interdigit electrodes (Figure 6B), the symmetric Pt-$Ni_3(HITP)_2$ / Pt-$Ni_3(HITP)_2$ microdevice is fabricated and the electrochemical performance are evaluated. To this end, pulsed potentiostatic deposition in MeOH-DMSO electrolytic bath was conducted, with an electrodeposition charge of 100 µC and of 400 µC applied on each Pt current collector (Figure S11). CV of the $Ni_3(HITP)_2$ micro-supercapacitor, measured in the voltage window of 0-1.0 V at 5 $V.s^{-1}$, displayed a combination of rectangular shape voltammogram with a redox peaks around ~ 0.5 V. This translates into higher current delivery (normalized to the footprint surface) as compared to the bare uncoated Pt / Pt MSC (Figure S12). Electrochemical impedance spectroscopy (EIS) analysis of bare and $Ni_3(HITP)_2$ coated electrodes displayed an increased sloppy nature of the Nyquist plot at lower frequencies, corroborating the capacitive nature of coated electrodes (Figure S13-A.). However, the high solution resistance (inset of Figure S13-A.) indicates the increased interfacial resistance of $Ni_3(HITP)_2$. Further, the frequency plot (Figure S13-B.) attests the preservation of capacitive behaviour up to a characteristic frequency of 1160.7 Hz. It also pinpoints a remarkable relaxation time constant, ν_0, of 0.9 ms, which signifies a high percentage of the useful capacitance inherent to $Ni_3(HITP)_2$ through a fast charging/discharging process. Importantly, a reduced value of ν_0 is indicative of faster ion transport within the electrode.

Detailed electrochemical performance analysis of $Ni_3(HITP)_2$ micro-supercapacitors was undertaken using cyclic voltammetry, at different scan rates in two different voltage ranges in 1.0 M KOH aqueous electrolyte. The rectangular-shaped voltammograms while cycling in the limited voltage window of 0 - 0.5 V indicates pure double-layer capacitive storage mechanism, with an average areal capacitance of 0.27 $mF.cm^{-2}$ (Figure S14). Conversely, when operated in a wider voltage window of 0 - 0.8 V, an additional reversible redox behaviour is noted coming from the redox activity of $Ni_3(HITP)_2$, with an increased average areal capacity of 0.48 $mF.cm^{-2}$ (Figure 6C). These reversible oxidation and reduction peaks, observed around ~0.6V and ~0.3V respectively, are attributed to the reversible redox process centered on the HATP ligand.[4] The large difference in potential between the oxidation and reduction peaks is certainly due to the ultra-high scan rates used for the CV measurement from 1 to 10 $V.s^{-1}$.

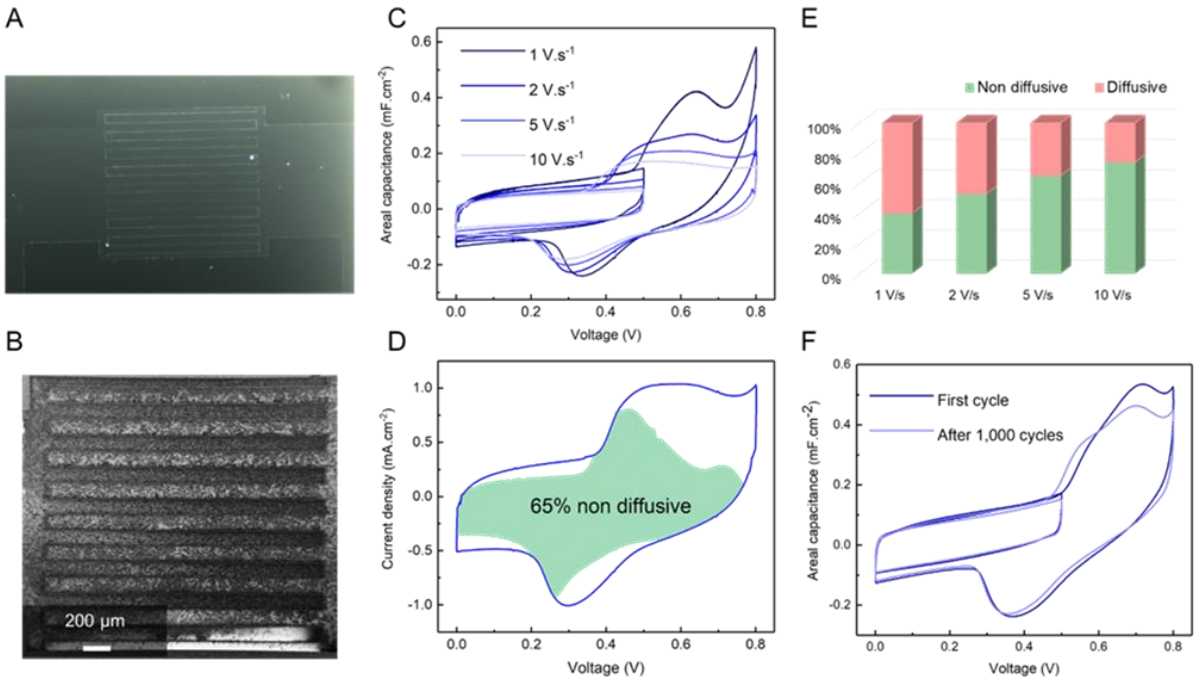

Figure 6. (A) Optical photograph of the interdigit electrodes, and (B) SEM image of $Ni_3(HITP)_2$ coated electrodes. (C) Cyclic voltammograms of $Ni_3(HITP)_2$ micro-supercapacitor in 1M KOH aqueous electrolyte at different scan rates. (D) Analysis of the cyclic voltammogram acquired at a scan rate of $5V.s^{-1}$, differentiating the non-diffusive current (shaded region) from the total current (blue line). (E) Histogram showing the percentage of non-diffusive nature contribution to the stored charge at different scan rates. (F) Cyclic voltammograms at scan rate of $5V.s^{-1}$ showing the stability of the device over 1.000 cycles.

To confirm the rate capability of the fabricated micro-supercapacitors, we studied kinetics limitation at the electrode level. From the kinetics analysis the $Ni_3(HITP)_2$ electrodes show an anodic $\boldsymbol{b}$-value of 0.63 and a cathodic $\boldsymbol{b}$-value of 0.87, testifying the heightened ion-diffusion limitation during anodic process relative to cathodic process (detailed analysis is provided as note to Figure S15 in SI). The non-diffusion contribution of $Ni_3(HITP)_2$ was quantified employing the power law (Figure S15).[71] The evaluation of the non-diffusion-limited coefficient $\boldsymbol{a_1}$ and diffusion-limited coefficient $\boldsymbol{a_2}$ (by mathematical considerations described in the caption of Figure S16) allows quantifying both diffusion and non-diffusion limited contributions. For instance, the cyclic voltammogram exhibit a non-diffusion behaviour of 65% at a scan rate of 5 $V.s^{-1}$ (shaded region, Figure 6D). This proportion amplifies at higher scan rates, reaching up to 75% at $10V.s^{-1}$ (Figure 6E) promoting fast redox process.

Finally, the stability of the $Ni_3(HITP)_2$ micro-supercapacitor was confirmed by performing CV experiments over 1.000 cycles at a scan rate of 5 $V.s^{-1}$, in both tested voltage windows of 0 – 0.5V and 0 – 0.8V (Figure 6F), with no visible change in the capacitive regimes (0 – 0.5V) observed, which indicates high stability of the device. Minor changes are noted the wide voltage

window (0 – 0.8V), albeit without losing the reversibility, further confirming the robustness and stability of the assembled $Ni_3(HITP)_2$ based micro-supercapacitors.

4. Conclusion

We demonstrated the non-sacrificial anodic deposition of homogeneous and crystalline $Ni_3(HITP)_2$ films on various current collectors for micro-supercapacitor applications. SEM analysis revealed the films morphologies constituted of aggregated $Ni_3(HITP)_2$ primary particles, collectively grown in homogeneous stable and thick films that can be integrated onto any desired conductive substrate. Applying pulsed deposition of $Ni_3(HITP)_2$ in MeOH-DMSO electrolytic bath proved to be the most suitable technique to prepare step-conformal crystalline films on various nanoarchitectured scaffolds. The optimized electrodeposition method was further successfully employed to fabricate nanoarchitectures, including $Pt@Ni_3(HITP)_2$ core-shell nanowires, nanotube networks, and uniformly coated fine-scale interdigit micro-supercapacitors. The microdevices exhibited good electrochemical performances and ultra-high rate capability. For future perspectives, the direct non-sacrificial anodic deposition approach of $Ni_3(HITP)_2$ could be extrapolated to accommodate conformal films of other MOFs with analogous functionalities such as hexaminobenzene structures. The method could be adapted to other conductive MOFs based on redox-active functionalized ligand, such as triphenylene (with functional O,O' ; N,N' ; S,S'), benzene (hexaoxy-, hexamino-, hexathiol-) and derivatives. Complementary, other centers could be used, by using transition metal (*e.g.* with Co, Ni, Fe, Cu ions) or lanthanide ions (*e.g.* La, Nd, Eu ions) that should be feasible vis the non-sacrifical route.[52,72] A compromise should be nevertheless found, particularly if both metal and ligand species are redox active (this being responsible for the formation of impure or multiphase materials). The parameters of electrodeposition are pivotal for each new MOF combination: the working potential, the composition of the electrolytic bath (nature and volume of solvents, metal:ligand ratio, nature and amount of additives such as base, the pH), the electrodeposition method, the substrate. Hence, the direct non-sacrificial anodic deposition method is considered to open doors towards the integration of conductive MOF films in advanced microelectronic applications.

Supporting Information

Supporting Information is available from the Wiley Online Library or from the author.

Acknowledgements

S.B, J.O, L.P and A.V. acknowledge the CF-ARC grant (18/23-093) MICROBAT for financial support. G.C. acknowledges the Belgian Fonds de la recherche scientifique (F.R.S.-FNRS) for FRIA fellowship. A.V. acknowledges funding from the European Research Council (ERC) grant-project 770870-MOOiRE. The authors acknowledge Dr. Fabien Drault for assisting D. M. with TEM analysis. The authors would like to thank the French National Research Agency (STORE-EX Labex Project ANR-10-LABX-76-01 and MEMPACAP ANR project). The French RENATECH network and the University of Lille are greatly acknowledged for supporting the Center of MicroNanoFabrication (CMNF) facility from IEMN. This work received funding from the CPER Hauts de France projects, IMITECH and MEL.

Dr. S. Behboudikhiavi and G. Chanteux equally contributed to this work.

Received: ((will be filled in by the editorial staff))
Revised: ((will be filled in by the editorial staff))
Published online: ((will be filled in by the editorial staff))

References

[1] J. Liu, X. Song, T. Zhang, S. Liu, H. Wen, L. Chen, *Angewandte Chemie - International Edition* **2021**, *60*, 5612–5624.

[2] R. A. Kharod, J. L. Andrews, M. Dincă, *Annu Rev Mater Res* **2022**, *52*, 103–128.

[3] W. Zhao, T. Chen, W. Wang, B. Jin, J. Peng, S. Bi, M. Jiang, S. Liu, Q. Zhao, W. Huang, *Sci Bull (Beijing)* **2020**, *65*, 1803–1811.

[4] D. Sheberla, J. C. Bachman, J. S. Elias, C. J. Sun, Y. Shao-Horn, M. Dincă, *Nat Mater* **2017**, *16*, 220–224.

[5] H. T. B. Pham, J. Y. Choi, S. Huang, X. Wang, A. Claman, M. Stodolka, S. Yazdi, S. Sharma, W. Zhang, J. Park, *J Am Chem Soc* **2022**, *144*, 10615–10621.

[6] F. Bu, W. Zhou, Y. Xu, Y. Du, C. Guan, W. Huang, *npj Flexible Electronics* **2020**, *4*.

[7] J. Han, Y. C. Lin, L. Chen, Y. C. Tsai, Y. Ito, X. Guo, A. Hirata, T. Fujita, M. Esashi, T. Gessner, M. Chen, *Advanced Science* **2015**, *2*, 1500067.

[8] K. H. Dinh, P. Roussel, C. Lethien, *ACS Omega* **2023**, *8*, 8977–8990.

[9] C. Lethien, J. Le Bideau, T. Brousse, *Energy Environ Sci* **2019**, *12*, 96–115.

[10] W. W. Liu, Y. Q. Feng, X. Bin Yan, J. T. Chen, Q. J. Xue, *Adv Funct Mater* **2013**, *23*, 4111–4122.

[11] W. Yu, H. Zhou, B. Q. Li, S. Ding, *ACS Appl Mater Interfaces* **2017**, *9*, 4597–4604.

[12] L. Liu, D. Ye, Y. Yu, L. Liu, Y. Wu, *Carbon N Y* **2017**, *111*, 121–127.

[13] M. Beidaghi, C. Wang, *Adv Funct Mater* **2012**, *22*, 4501–4510.

[14] K. Jiang, I. A. Baburin, P. Han, C. Yang, X. Fu, Y. Yao, J. Li, E. Cánovas, G. Seifert, J. Chen, M. Bonn, X. Feng, X. Zhuang, *Adv Funct Mater* **2020**, *30*, 1908243.

[15] H. Hu, K. Zhang, S. Li, S. Ji, C. Ye, *J Mater Chem A Mater* **2014**, *2*, 20916–20922.

[16] X. Wang, Y. Yin, X. Li, Z. You, *J Power Sources* **2014**, *252*, 64–72.

[17] M. Xue, Z. Xie, L. Zhang, X. Ma, X. Wu, Y. Guo, W. Song, Z. Li, T. Cao, *Nanoscale* **2011**, *3*, 2703–2708.

[18] B. Bounor, B. Asbani, C. Douard, F. Favier, T. Brousse, C. Lethien, *Energy Storage Mater* **2021**, *38*, 520–527.

[19] E. Eustache, C. Douard, A. Demortière, V. De Andrade, M. Brachet, J. Le Bideau, T. Brousse, C. Lethien, *Adv Mater Technol* **2017**, *2*, 1700126.

[20] B. Asbani, K. Robert, P. Roussel, T. Brousse, C. Lethien, *Energy Storage Mater* **2021**, *37*, 207–214.

[21] A. Jrondi, G. Buvat, F. D. La Pena, M. Marinova, M. Huvé, T. Brousse, P. Roussel, C. Lethien, *Adv Energy Mater* **2023**, *13*, 2203462.

[22] K. Robert, D. Stiévenard, D. Deresmes, C. Douard, A. Iadecola, D. Troadec, P. Simon, N. Nuns, M. Marinova, M. Huvé, P. Roussel, T. Brousse, C. Lethien, *Energy Environ Sci* **2020**, *13*, 949–957.

[23] Y. Li, H. Xie, J. Li, Y. Bando, Y. Yamauchi, J. Henzie, *Carbon N Y* **2019**, *152*, 688–696.

[24] G. Genesio, J. Maynadié, M. Carboni, D. Meyer, *New Journal of Chemistry* **2018**, *42*, 2351–2363.

[25] Z. Zhuang, D. Liu, *Nanomicro Lett* **2020**, *12*, 1–32.

[26] X. Mu, W. Wang, C. Sun, J. Wang, C. Wang, M. Knez, *Adv Mater Interfaces* **2021**, *8*, 2002151.

[27] J. Liu, Y. Chen, X. Feng, R. Dong, *Small Struct* **2022**, *3*, 2100210.

[28] M. Wang, H. Shi, P. Zhang, Z. Liao, M. Wang, H. Zhong, F. Schwotzer, A. S. Nia, E. Zschech, S. Zhou, S. Kaskel, R. Dong, X. Feng, *Adv Funct Mater* **2020**, *30*, 2002664.

[29] R. Zheng, Z. H. Fu, W. H. Deng, Y. Wen, A. Q. Wu, X. L. Ye, G. Xu, *Angewandte Chemie - International Edition* **2022**, *61*, e202212797.

[30] G. Wu, J. Huang, Y. Zang, J. He, G. Xu, *J Am Chem Soc* **2017**, *139*, 1360–1363.

[31] M. Zhang, B. H. Zheng, J. Xu, N. Pan, J. Yu, M. Chen, H. Cao, *Chemical Communications* **2018**, *54*, 13579–13582.

[32] F. J. Claire, M. A. Solomos, J. Kim, G. Wang, M. A. Siegler, M. F. Crommie, T. J. Kempa, *Nat Commun* **2020**, *11*, 5524.

[33] V. Rubio-Giménez, G. Arnauts, M. Wang, E. S. Oliveros Mata, X. Huang, T. Lan, M. L. Tietze, D. E. Kravchenko, J. Smets, N. Wauteraerts, A. Khadiev, D. V. Novikov, D. Makarov, R. Dong, R. Ameloot, *J Am Chem Soc* **2022**, *145*, 152–159.

[34] Y. Liu, Y. Wei, M. Liu, Y. Bai, X. Wang, S. Shang, J. Chen, Y. Liu, *Angewandte Chemie - International Edition* **2021**, *60*, 2887–2891.

[35] S. A. Lee, J. W. Yang, S. Choi, H. W. Jang, *Exploration* **2021**, *1*, 20210012.

[36] B. Asbani, G. Buvat, J. Freixas, M. Huvé, D. Troadec, P. Roussel, T. Brousse, C. Lethien, *Energy Storage Mater* **2021**, *42*, 259–267.

[37] X. Zhang, K. Wan, P. Subramanian, M. Xu, J. Luo, J. Fransaer, *J Mater Chem A Mater* **2020**, *8*, 7569–7587.

[38] V. M. V., G. Nageswaran, *J Electrochem Soc* **2020**, *167*, 155527.

[39] S. A. Lee, J. W. Yang, S. Choi, H. W. Jang, *Exploration* **2021**, *1*, 20210012.

[40] S. Xie, Z. Zhou, X. Zhang, J. Fransaer, *Chem Soc Rev* **2023**, *52*, 4292–4312.

[41] M. Li, M. Dincă, *Chem Sci* **2014**, *5*, 107–111.

[42] M. Li, M. Dincă, *J Am Chem Soc* **2011**, *133*, 12926–12929.

[43] S. Xie, W. Monnens, K. Wan, W. Zhang, W. Guo, M. W. Xu, I. F. J. Vankelecom, X. Zhang, J. Fransaer, *Angewandte Chemie - International Edition* **2021**, *60*, 24950–24957.

[44] P. Li, X. Shi, Y. Wu, M. Song, Y. Lai, H. Yu, G. Lu, *CrystEngComm* **2021**, *23*, 1828–1835.

[45] Y. Liu, Y. Wei, M. Liu, Y. Bai, X. Wang, S. Shang, J. Chen, Y. Liu, *Angewandte Chemie - International Edition* **2021**, *60*, 2887–2891.

[46] M. De Lourdes Gonzalez-Juarez, E. Flores, M. Martin-Gonzalez, I. Nandhakumar, D. Bradshaw, *J Mater Chem A Mater* **2020**, *8*, 13197–13206.

[47] M. De Lourdes Gonzalez-Juarez, C. Morales, J. I. Flege, E. Flores, M. Martin-Gonzalez, I. Nandhakumar, D. Bradshaw, *ACS Appl Mater Interfaces* **2022**, *14*, 12404–12411.

[48] H. Jia, S. Lu, S. H. Ra Shin, M. L. Sushko, X. Tao, M. Hummel, P. K. Thallapally, J. Liu, Z. Gu, *J Power Sources* **2022**, *526*, 231163.

[49] N. Campagnol, T. R. C. Van Assche, M. Li, L. Stappers, M. Dinca, J. F. M. Denayer, K. Binnemans, D. E. De Vos, J. Fransaer, *J Mater Chem A Mater* **2016**, *4*, 3914–3925.

[50] T.-N. Pham-Truong, H. Guemiza, H. Lavillunière, C. Vancaeyzeele, P.-H. Aubert, *Electrochim Acta* **2023**, *441*, 141792.

[51] X. Zhang, K. Wan, P. Subramanian, M. Xu, J. Luo, J. Fransaer, *J Mater Chem A Mater* **2020**, *8*, 7569–7587.

[52] M. Song, J. Jia, P. Li, J. Peng, X. Pang, M. Qi, Y. Xu, L. Chen, L. Chi, G. Lu, *J Am Chem Soc* **2023**, *145*, 25570–25578.

[53] F. Feigl, M. Fürth, *Monatsh Chem* **1927**, *48*, 445–450.

[54] E. I. Stiefel, J. H. Waters, E. Billig, H. B. Gray, *J Am Chem Soc* **1965**, *87*, 3016–3017.

[55] G. S. Hall, R. H. Soderberg, *Inorg Chem* **1968**, *7*, 2300–2303.

[56] D. Sheberla, L. Sun, M. A. Blood-Forsythe, S. Er, C. R. Wade, C. K. Brozek, A. Aspuru-Guzik, M. Dincă, *J Am Chem Soc* **2014**, *136*, 8859–8862.

[57] T. Chen, J. H. Dou, L. Yang, C. Sun, N. J. Libretto, G. Skorupskii, J. T. Miller, M. Dincă, *J Am Chem Soc* **2020**, *142*, 12367–12373.

[58] F. Zivari-Moshfegh, D. Nematollahi, M. M. Khoram, A. Rahimi, *Electrochim Acta* **2020**, *354*, 136700.

[59] M. Pelmus, E. M. Ungureanu, M. D. Stanescu, L. Tarko, *J Appl Electrochem* **2020**, *50*, 851–862.

[60] S. Laschat, A. Baro, N. Steinke, F. Giesselmann, C. Hägele, G. Scalia, R. Judele, E. Kapatsina, S. Sauer, A. Schreivogel, M. Tosoni, *Angewandte Chemie - International Edition* **2007**, *46*, 4832–4887.

[61] I. L. Eisgruber, J. R. Engel, R. E. Hollingsworth, P. K. Bhat, R. Wendt, *Journal of Vacuum Science & Technology A: Vacuum, Surfaces, and Films* **1999**, *17*, 190–197.

[62] B. Bounor, B. Asbani, C. Douard, D. Deresmes, D. Stiévenard, P. Roussel, F. Favier, C. Lethien, T. Brousse, *J Electrochem Soc* **2023**, *170*, 030530.

[63] A. John, A. Saeed, Z. A. Khan, *Materials* **2023**, *16*, 2192.

[64] S. Wahyudi, S. Soepriyanto, M. Z. Mubarok, Sutarno, *IOP Conf Ser Mater Sci Eng* **2019**, *547*, 012020.

[65] A. S. Elmezayyen, S. Guan, F. M. Reicha, I. M. El-Sherbiny, J. Zheng, C. Xu, *J Phys D Appl Phys* **2015**, *48*, 175502.

[66] W. Wang, M. Tian, A. Abdulagatov, S. M. George, Y.-C. Lee, R. Yang, *Nano Lett* **2012**, *12*, 655–660.

[67] P. L. Taberna, S. Mitra, P. Poizot, P. Simon, J.-M. Tarascon, *Nat Mater* **2006**, *5*, 567–573.

[68] B. Asbani, G. Buvat, J. Freixas, M. Huvé, D. Troadec, P. Roussel, T. Brousse, C. Lethien, *Energy Storage Mater* **2021**, *42*, 259–267.

[69] X. Li, Y. Wang, G. Song, Z. Peng, Y. Yu, X. She, J. Li, *Nanoscale Res Lett* **2009**, *4*, 1015–1020.

[70] A. H. Jo, S. Y. Kim, J. H. Kim, Y. A. Kim, C.-M. Yang, *Int J Energy Res* **2023**, *2023*, 1–13.

[71] J. Wang, J. Polleux, J. Lim, B. Dunn, *Journal of Physical Chemistry C* **2007**, *111*, 14925–14931.

[72] L. S. Xie, G. Skorupskii, M. Dincă, *Chem Rev* **2020**, *120*, 8536–8580.

Title : Direct Electrodeposition of Electrically Conducting $Ni_3(HITP)_2$ MOF Nanostructures for Micro-Supercapacitor Integration

TOC Summary : Direct anodic and non-sacrificial electrochemical deposition of an electrically conducting MOF Ni_3HITP_2, on a variety of metallic, semiconducting and carbon substrates, with fine control over nanostructured architectures is reported. Ni_3HITP_2 MOF is integrated within micro-supercapacitor interdigit device, using the method developed thereof, with enhanced capacitive storage and cycling stability.